Computer Physics Communications 305 (2024) 109327

Contents lists available at ScienceDirect

Computer Physics Communications

journal homepage: www.elsevier.com/locate/cpc

Computer Programs in Physics

libEMMI_MGFD: A program of marine controlled-source electromagnetic modelling and inversion using frequency-domain multigrid solver ☆

Pengliang Yang *, An Ping

School of Mathematics, Harbin Institute of Technology, 150001, China

ARTICLE INFO

Keywords:
Frequency domain modelling
Geometrical multigrid (GMG)
Controlled-source electromagnetics (CSEM)
Resistivity tomography
Reverse communication

ABSTRACT

We develop a software package libEMMI_MGFD for 3D frequency-domain marine controlled-source electromagnetic (CSEM) modelling and inversion. It is the first open-source C program tailored for geometrical multigrid (GMG) CSEM simulation. An volumetric anisotropic averaging scheme has been employed to compute effective medium for modelling over uniform and nonuniform grid. The computing coordinate is aligned with acquisition geometry by rotation with the azimuth and dip angles, facilitating the injection of the source and the extraction of data with arbitrary orientations. Efficient nonlinear optimization is achieved using quasi-Newton scheme assisted with bisection backtracking line search. In constructing the modularized Maxwell solver and evaluating the misfit and gradient for 3D CSEM inversion, the reverse communication technique is the key to the compaction of the software while maintaining the computational performance. A number of numeric tests demonstrate the efficiency of the modelling while preserving the solution accuracy. A 3D marine CSEM inversion example has been examined for resistivity imaging.

PROGRAM SUMMARY

Program Title: libEMMI_MGFD
CPC Library link to program files: https://doi.org/10.17632/mpk7xrd38m.1
Developer's repository link: https://github.com/yangpl/libEMMI_MGFD
Licensing provisions: GNU General Public License v3.0
Programming language: C, Shell
Software dependencies: MPI [1]
Nature of problem: 3D Controlled-source electromagnetic modelling and inversion.
Solution method: Frequency-domain modelling on staggered grid; Geometrical multigrid (GMG) method as an iterative solver; Quasi-Newton method for nonlinear minimization; Bisection-based backtracking line search.

References

[1] https://www.mpich.org/.

1. Introduction

Controlled-source electromagnetic (CSEM) modelling and inversion have emerged as invaluable tools in understanding subsurface geological structures and resource exploration. This technique utilizes controlled electromagnetic sources, typically deployed on the seafloor or land surface, to probe the Earth's subsurface. By analyzing the response of the Earth's electrical conductivity to these electromagnetic signals, CSEM enables the detection and characterization of various subsurface features, including hydrocarbon reservoirs, mineral deposits, and geological formations [1,2].

A variety of algorithms and computing techniques have been routinely employed for electromagnetic modelling, e.g., finite difference method in frequency domain [3–6] and in time domain [7–10], as well as finite element method in frequency domain [11–14]. The discretization of the frequency-domain Maxwell equation in 3D leads to a linear system possessing extremely large number of unknowns. Solution of such a linear system is computationally intensive and storage demanding. The use of direct solver to solve the diffusive Maxwell equation

☆ The review of this paper was arranged by Prof. David W. Walker.
* Corresponding author.
E-mail addresses: ypl.2100@gmail.com (P. Yang), 2021110084@stu.hit.edu.cn (A. Ping).

https://doi.org/10.1016/j.cpc.2024.109327
Received 30 April 2024; Received in revised form 23 June 2024; Accepted 26 July 2024
Available online 29 July 2024

is straightforward [6,15], but may require significant amount of computer memory, which is rather challenging if the size of the problem becomes prohibitively large. The iterative methods such as QMR [3,16], BICGSTAB [17], GMRES [18] and multigrid [5,19,20] algorithms are commonplaces to alleviate memory issues, but may suffer from convergence difficulties due to the ill-conditioning of the linear system [21,22].

CSEM inversion, sometimes referred to as resistivity imaging, plays a crucial role in CSEM data interpretation by reconstructing subsurface conductivity/resistivity distributions from measured electromagnetic field data. Using efficient modelling engines, inversion algorithms seek to minimize the difference between observed and predicted electromagnetic data by iteratively adjusting model parameters, such as subsurface conductivity values. This iterative optimization process aims to find the most plausible subsurface conductivity distribution that best fits the observed data, thereby providing valuable insights into subsurface structures and properties.

There have been a large number of open software for electromagnetic modelling and inversion, e.g. `SimPEG` [23], `MARE2DEM` [13], pyGIMLI [24], `emg3d` [25], `custEM` [14], ResIPy [26], just to name a few. Among them, some of them are dedicated to marine CSEM, for example, `MARE2DEM` and `emg3d`. We aim to make some relevant contributions in this aspect, by developing a standalone software `libEMMI_MGFD` for 3D large scale problems in high performance parallel computing settings.

- Different from our previous code `libEMMI` [22] computing frequency domain responses via time-domain modelling, the core modelling engine of this package solves diffusive Maxwell equation discretized in the frequency domain. Inspired by the optimal convergence within $O(N)$ complexity, we re-implemented the geometrical multigrid (GMG) modelling of 3D CSEM data proposed by [5] in C programming language, following the `emg3d` code in Python [25].
- The goal of CSEM inversion is to retrieve resistivity anomaly starting from a crude initial guess by data driven approaches. Due to the high dimensionality of the parameter space, it is infeasible to use global optimization methods to fit such a parametric model. Local optimization with quasi-Newton and Newton type method naturally becomes the method of choice.
- The software has been carefully designed thanks to the reverse communication strategy. It provides a succinct yet reliable mechanism to modularize the GMG linear solver and the code blocks for function and gradient evaluation which are frequently used in every iteration of the nonlinear inversion. Based on such a concept, the LBFGS algorithm combined with bisection-based backtracking line search are coded compactly.

Despite the fact that modelling EM diffusion using GMG by [5] and the LBFGS-based CSEM inversion [27] are known, we highlight that binding these components into to construct a complete set of parallel and efficient open source software in C is still worthwhile for a large number of computational geophysicists to do further development.

2. Methodology

2.1. CSEM forward problem

The physics of controlled-source electromagnetic (CSEM) technology is governed by diffusive Maxwell equation, consisting of Faraday's law and Ampère's law. The two laws combined with proper boundary condition forms a set of partial differential equation (PDE) in the frequency domain

$$\nabla \times E - \mathrm{i}\omega\mu H = M_s, \tag{1a}$$

$$\nabla \times H - \sigma E = J_s, \tag{1b}$$

where the electrical field $E = (E_x, E_y, E_z)^{\mathrm{T}}$ and the magnetic field $H = (H_x, H_y, H_z)^{\mathrm{T}}$ are excited by source current $J_s = (J_x, J_y, J_z)^{\mathrm{T}}$ and $M_s = (M_x, M_y, M_z)^{\mathrm{T}}$ based on the electric conductivity σ and magnetic permeability μ. In practical applications, we consider vanishing magnetic source and constant magnetic permeability, that is, $M_s = 0$ and $\mu = \mu_r\mu_0 = 4\pi \times 10^{-7}$ H/m (with $\mu_r = 1$). In the above, Fourier transform convention $\partial_t \leftrightarrow -\mathrm{i}\omega$ with ω being the angular frequency has been adopted.

By eliminating the magnetic field H, the Maxwell equation translates into

$$\nabla \times \mu_r^{-1} \nabla \times E - \mathrm{i}\omega\mu_0\sigma E = \mathrm{i}\omega\mu_0 J_s + \nabla \times \mu_r^{-1} M_s. \tag{2}$$

Equation (2) can be viewed as a complex-valued linear system

$$AE = b, \tag{3}$$

where $A = \nabla \times \mu_r^{-1} \nabla \times -\mathrm{i}\omega\mu_0\sigma$, $b = \mathrm{i}\omega\mu_0 J_s + \nabla \times \mu_r^{-1} M_s$. The electrical field E is obtained from the solution of the above linear system using direct or iterative solvers. Away from sources, the magnetic field H can then be computed from equation (1a)

$$H = (\mathrm{i}\omega\mu)^{-1} \nabla \times E. \tag{4}$$

2.2. Frequency-domain geometrical multigrid modelling

To make the meshing simple, equation (2) has been discretized on a nonuniform cartesian grid. We choose the geometrical multigrid (GMG) method for the numerical modelling of diffusive Maxwell equation in the frequency domain, inspired by its optimal convergence properties [28]. The core idea of GMG is simple:

- The high frequency components of the residual of the PDE can be effectively removed using few number of smoothing steps (called relaxation), e.g., Gauss-Seidel algorithm;
- The low frequency components of the residual of the PDE can then be transformed to higher frequency components by mapping them onto a coarse grid (it is coined restriction);
- The solution at the coarse grid must be mapped back to fine grid as a correction to the approximate solution at the fine grid in a bottom-to-top fashion (it is coined prolongation or interpolation), to obtain a better approximation of the true solution of the equation;
- By cascading these steps in a multiscale manner, all frequency components of the residual are expected to be reduced effectively, leading to a significantly refined solution to the PDE.

A full chain of the recursion involving multiple grid levels is called V cycle. To further improve the efficiency of error smoothing, W and F cycles can then be constructed using the basic V cycles. The residual of the equation vanishes after a number of V, W or F cycles. Fig. 1 schematically illustrates the computing steps of V, W and F cycles based on recursion among 4 grid levels.

Since $\nabla \times E = \nabla \times (E + \nabla V)$ is valid for any scalar potential field V, the solution of the above linear system is therefore non-unique due to the null space of the curl-curl operator, in case the second term on the left hand side of equation (2) is extremely small. This is exactly the case when the frequency is very low ($\omega \approx 0$) and the conductivity is negligible ($\sigma \approx 0$, it is typically the case in the air). This leads to a highly ill-conditioned linear system, making the iterative methods difficult to converge. Preconditioning is therefore designed to rectify the poor convergence, using divergence correction [17] or Helmholtz decomposition (also known as A-ϕ potential field decomposition) with Coulomb [29] or Lorentz gauge [30]. We apply the preconditioning in the process of Gauss-Seidel smoothing, which is the key to the success of GMG in solving diffusive Maxwell equation. A pointwise Gauss-Seidel sweeping in a lexicographic order has been applied following the proposal of [5]. At each point, a 6×6 linear system is solved using LU decomposition. The

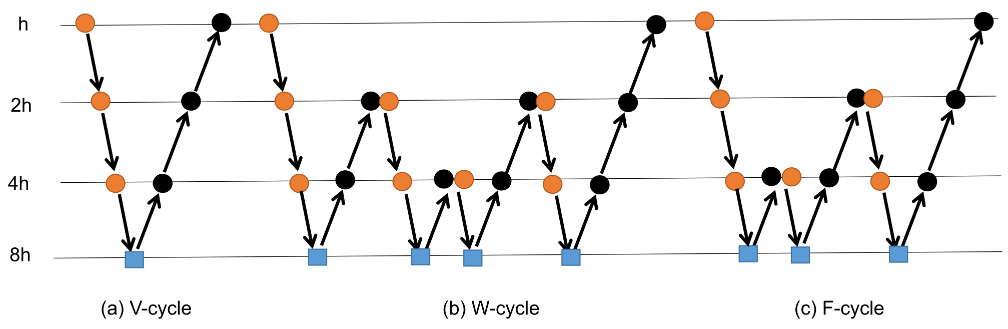

Fig. 1. Schematic illustration of (a) V cycle, (b) W cycle and (c) F cycle based on 4 grid levels. The jth grid level corresponds to a discretized cell size $2^j h$ ($j = 0$ corresponds to the finest grid). The arrow downwards $\searrow$ indicates a restriction from the fine grid $2^{j-1}h$ to the fine grid $2^j h$, while the arrow upwards $\nearrow$ indicates a prolongation from the fine grid $2^j h$ to the coarse grid $2^{j-1}h$. The orange and black dots stand for pre- and post-smoothing operations. The blue square at the coarsest grid corresponds to direct solve, which is often done by several times of smoothing. (For interpretation of the colours in the figure(s), the reader is referred to the web version of this article.)

updated electrical field is then injected as the right hand side for the solution of the next 6×6 linear system. Indeed, this block Gauss-Seidel iteration is nothing else than the multiplicative Schwarz preconditioning [31, chapter 14.3]. Recall that the key idea of preconditioning is to approximately solve the linear system cheaply as effective as possible, the Gauss-Seidel smoothing overcomes the ill-conditioning of the linear system in (3).

The use of nonuniform grid creates certain amount of numerical anisotropy which makes multigrid iterations converge slowly. A line Gauss-Seidel scheme combined with semi-coarsening (halving the number of gridpoints in only two directions in 3D when mapping the residual from fine to coarse grid) is a useful recipe to deal with this problem, by combining all 6×6 small linear systems to construct a larger one along x, y and z axes. From a domain decomposition point of view, each linear system along a line forms a subdomain to partition the full 3D grid. Since the number of unknowns are much larger, we resort to incomplete LU (ILU) (instead of Cholesky factorization as done by [5]) to solve it: the intermediate elements created during ILU are stored in place thanks to the compressed diagonal storage (CDS) technique [32]. Compared with the 6×6 block, the size of the linear system along a line is much closer to the full 3D grid. Consequently, it is expected to supply a better approximation of the full linear system, leading to faster convergence rate. We refer to [33, chapter 3.1.2] to check out more details on building up the linear system for block and line Gauss-Seidel smoothing.

2.3. Regridding over the effective medium

The accuracy of the modelling engine is generally higher on a dense mesh than that on a coarse mesh. This however significantly increases the computational cost, since the number of grid points to discretize the same physical domain grows quickly with refined grid spacing. Nonuniform grid has been widely adopted to reduce the computational cost. To achieve efficient CSEM modelling, the grid spacing in regions demanding high modelling accuracy is made to be small, while the grid spacing in other regions is taken to be large. `libEMMI_MGFD` adopts the power-law grid stretching [5, Appendix C]: the grid size gradually increases away from the source following a geometric progression. To simulate EM fields propagating to very far distance using limited mesh size, we extend the domain of interest six skin depth, such that the amplitude goes further down to $e^{-6} = 0.25\%$ to avoid boundary effect. The generation of the nonuniform grid after domain extension follows the fixed point iteration algorithm in [21].

To map the input parameters to modelling grid, we perform volume average for the horizontal conductivities σ_{xx}, σ_{yy} and vertical resistivity σ_{zz}^{-1} for multigrid modelling. The averaged values at the cell centre $(x_{i+0.5}, y_{j+0.5}, z_{k+0.5})$ are computed

$$\bar{\sigma}_{xx}(x_{i+0.5}, y_{j+0.5}, z_{k+0.5}) = \frac{1}{\bar{V}_{i+0.5,j+0.5,k+0.5}} \int_{x_i}^{x_{i+1}} \int_{y_j}^{y_{j+1}} \int_{z_j}^{z_{j+1}} \sigma_{xx}(x, y, z) \mathrm{d}x\mathrm{d}y\mathrm{d}z, \tag{5a}$$

$$\bar{\sigma}_{yy}(x_{i+0.5}, y_{j+0.5}, z_{k+0.5}) = \frac{1}{\bar{V}_{i+0.5,j+0.5,k+0.5}} \int_{x_j}^{x_{j+1}} \int_{y_j}^{y_{j+1}} \int_{z_j}^{z_{j+1}} \sigma_{yy}(x, y, z) \mathrm{d}x\mathrm{d}y\mathrm{d}z, \tag{5b}$$

$$\bar{\sigma}_{zz}(x_{i+0.5}, y_{j+0.5}, z_{k+0.5}) = \left(\frac{1}{\bar{V}_{i+0.5,j+0.5,k+0.5}} \int_{x_j}^{x_{j+1}} \int_{y_j}^{y_{j+1}} \int_{z_k}^{z_{k+1}} \sigma_{zz}^{-1}(x, y, z) \mathrm{d}x\mathrm{d}y\mathrm{d}z \right)^{-1} \tag{5c}$$

over the cell volume $\bar{V}_{i+0.5,j+0.5,k+0.5} = (x_{i+1} - x_i)(y_{i+1} - y_i)(z_{i+1} - z_i)$. It can be implemented by tensorial product of averaging in each direction. A simple and efficient way of the above averaging for every grid cell is to difference the integral starting from a reference origin (x_0, y_0, z_0). In 1D case, it corresponds to $\int_{x_i}^{x_{i+1}} = \int_{x_0}^{x_{i+1}} - \int_{x_0}^{x_i}$. The above VTI anisotropic averaging relies on the fact that the tangential fields see the resistors connected in parallel, while the normal field sees the resistors connected in series [34].

2.4. CSEM inverse problem

The CSEM inversion performs least-squares minimization between the observed EM data $d = (d_E, d_H)^{\mathrm{T}}$ and the synthetic data extracted from the simulated EM field $u = (E, H)^{\mathrm{T}}$. The total objective function incorporating the data misfit and a model regularization term is specified by

$$f(m) = \underbrace{\frac{1}{2}\|W_d(d - Ru)\|^2}_{f_d(m)} + \underbrace{\frac{\beta}{2}\|W_m(m - m_{ref})\|^2}_{f_m(m)}, \tag{6}$$

where the inversion parameter m is a function of electrical conductivity σ; R is the restriction operator mapping the EM field from the full domain to recording locations prescribed by the receivers. The penalty parameter β balances the data misfit term $f_d(m)$ and the model misfit $f_m(m)$; W_d and W_m are weighting matrices related to the data uncertainty and the model roughness. To minimize the objective function, we often consider a quadratic approximation of the original misfit function perturbed by a model increment δm

$$f(m + \delta m) \approx f(m) + \frac{\partial f(m)}{\partial m} \cdot \delta m + \frac{1}{2}\delta m \cdot \frac{\partial^2 f(m)}{\partial m^2} \cdot \delta m \tag{7}$$

To find the optimal δm allowing the misfit attaining its minimum, we require $\partial f(m+\delta m)/\partial\delta m = 0$, yielding the amount of model perturbation

$$\delta m = -\left(\frac{\partial^2 f(m)}{\partial m^2}\right)^{-1}\frac{\partial f(m)}{\partial m}, \tag{8}$$

where $\partial^2 f(m)/\partial m^2$ is the Hessian matrix. Assuming a symmetric positive definite (SPD) Hessian, equation (8) can be solved using conjugate gradient (CG) method, leading to the so-called Newton-CG method which is computationally expensive [35]. The quasi-Newton LBFGS algorithm [36] approximates the inverse Hessian based on gradient of the misfit $\partial f(m)/\partial m$. It consists of the first derivatives of $f_d(m)$ and $f_m(m)$ with respect to m

$$\frac{\partial f_d(m)}{\partial m} = \Re\langle W_d R\frac{\partial u}{\partial m}, W_d(Ru-d)\rangle, \tag{9a}$$

$$\frac{\partial f_m(m)}{\partial m} = \beta W_m^{\mathrm{T}} W_m(m-m_{ref}), \tag{9b}$$

where $\Re$ takes the real part of a complex value. Our CSEM inversion takes the logarithm of the resistivity ($\rho := 1/\sigma$ is the inverse of conductivity) as the inversion parameter, that is, $m = \ln\rho$. Here, the gradient of the data misfit in equation (9a) with respect to conductivity σ can be computed using the adjoint state method [22,37]

$$\frac{\partial f_d(m)}{\partial \sigma} = -\Re\sum_{\omega}\underline{\bar{E}}^{\mathrm{T}}\cdot E, \tag{10}$$

where the overbar takes the complex conjugate of a complex number; $\underline{\bar{E}}$ is the so-called adjoint electrical field satisfying the following equation

$$\nabla\times\mu^{-1}\nabla\times\underline{\bar{E}} - \mathrm{i}\omega\mu_0\sigma\underline{\bar{E}} = \mathrm{i}\omega\mu_0\overline{\delta d_E} + \nabla\times\mu_r^{-1}\overline{\delta d_H}, \tag{11}$$

where $\delta d_E = R^{\mathrm{T}}W_{d_E}^{\mathrm{T}}W_{d_E}(d_E - RE)$ and $\delta d_H = R^{\mathrm{T}}W_{d_H}^{\mathrm{T}}W_{d_H}(d_H - RH)$ are the electrical and magnetic components of the data residuals weighted by $W_d = \mathrm{diag}(W_{d_E}, W_{d_H})$. The adjoint equation (11) is of exactly the same form as the forward equation (2) except that the conjugation of the data residuals $\overline{\delta d_E}$ and $\overline{\delta d_H}$ replaces the role of J_s and M_s, implying that the same modelling engine can be used to compute the adjoint field $\underline{\bar{E}}$.

Since the CSEM data varies several order of magnitude within several kilometers offset, the normalization of the CSEM data plays a crucial role for the success of the inversion, based on the measurement uncertainty of the acquired electrical and magnetic fields. Taking into account the imperfection of the instruments and the ambient noise in the real acquisition, a practical value is around 3%, while the noise floor for electrical field and magnetic field is approximately $n_E = 10^{-15}$ V/m and $n_H = 10^{-13}$ Tesla [38]. The data weighting matrix W_d is then taken to be a diagonal matrix, with the diagonal elements being the inverse of the uncertainty.

2.5. Coordinate transformation

The computing coordinate used for numerical modelling and the original coordinate used for data acquisition are normally not the same. As shown in Fig. 2, the EM data in the computing coordinate (x,y,z) can be aligned with the acquisition coordinate (x',y',z') by first rotating along $x-y$ plane up to an azimuth angle ϕ, and then along z axis with a dip angle θ. As a result, the field $F = E, H$ in the two coordinate systems can be related to each other through

$$\begin{bmatrix}F_{x'}\\F_{y'}\\F_{z'}\end{bmatrix} = C\begin{bmatrix}F_x\\F_y\\F_z\end{bmatrix}, \tag{12}$$

where the rotation matrix is specified by

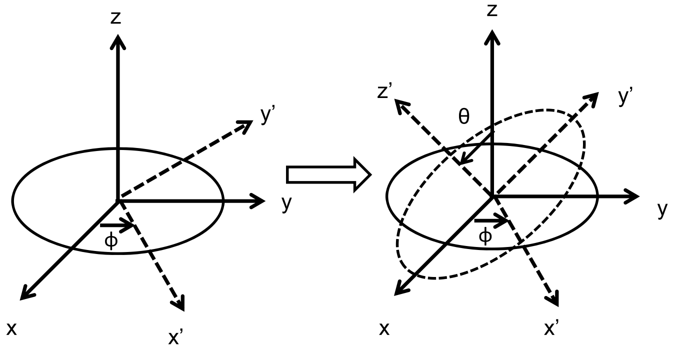

Fig. 2. The EM data can be aligned with the computing coordinate (x,y,z) by rotation of the data in the acquisition coordinate (x',y',z') along $x-y$ plane up to an azimuth angle ϕ first, and then along z axis with a dip angle θ.

$$\begin{aligned} C &= \begin{bmatrix}1&0&0\\0&\cos\theta&\sin\theta\\0&-\sin\theta&\cos\theta\end{bmatrix}\begin{bmatrix}\cos\phi&\sin\phi&0\\-\sin\phi&\cos\phi&0\\0&0&1\end{bmatrix}\\ &= \begin{bmatrix}\cos\phi&\sin\phi&0\\-\sin\phi\cos\theta&\cos\phi\cos\theta&\sin\theta\\\sin\phi\sin\theta&-\cos\phi\sin\theta&\cos\theta\end{bmatrix}. \end{aligned} \tag{13}$$

Equation (12) supplies a recipe to extract the modelling data in the computing grid to correctly match the observation coordinate.

Conversely, one can convert the fields from the acquisition coordinate (x',y',z') to the computing coordinate (x,y,z) via

$$\begin{bmatrix}F_x\\F_y\\F_z\end{bmatrix} = C^{-1}\begin{bmatrix}F_{x'}\\F_{y'}\\F_{z'}\end{bmatrix}, \tag{14}$$

where

$$C^{-1} = C^T = \begin{bmatrix}\cos\phi&-\sin\phi\cos\theta&\sin\phi\sin\theta\\\sin\phi&\cos\phi\cos\theta&-\cos\phi\sin\theta\\0&\sin\theta&\cos\theta\end{bmatrix}. \tag{15}$$

Equation (14) allows us to inject the EM sources in the original acquisition coordinate into the computing grid.

3. Software implementation

The `libEMMI_MGFD` code inherits a significant number of features from our fictitious wave domain CSEM imaging software `libEMMI` [22,34] and the seismic full waveform inversion (FWI) software `SMIwiz` [39]. The pointers associated with specific data structures are widely used in `libEMMI_MGFD`, in order to parse the parameters succinctly and pass them into dedicated subroutines for computation. A pointer of type `acq_t` holds the information related to the data acquisition geometry. A pointer of type `emf_t` indexes all information of electromagnetic field for forward and adjoint modelling. A pointer of type `fwi_t` is designed for inversion purposes (here we interpret EM inversion as full waveform inversion based on the electromagnetic equation). A pointer of type `opt_t` is dedicated to do nonlinear optimization. The interested reader is referred to `libEMMI` and `SMIwiz` for a detailed description of the common features aforementioned.

In the following, we focus on a modularized programming of an iterative solution of frequency-domain Maxwell equation using multigrid method in `libEMMI_MGFD`, which clearly differs from `libEMMI` modelling based on the fictitious wave domain time stepping scheme [21]. We code quasi-Newton LBFGS algorithm using bisection line search in the C programming language. The key to achieving an efficient and successful implementation is the use of reverse communication.

3.1. Recursive V, W and F cycles

We define a data of type gmg_t to encapsulate the grid and medium properties of 3D EM fields used in geometrical multigrid modelling:

```
typedef struct{
  int n1, n2, n3;//number of cells along x, y and z
  double *x1, *x2, *x3;//nodes along x, y and z
  double *x1s, *x2s, *x3s;//staggered nodes along x, y and z
  double *d1, *d2, *d3;//cell sizes \xch{centred}{centered} at integer nodes
  double *d1s, *d2s, *d3s;//cell sizes \xch{centred}{centered} at staggered nodes
  complex ****u, ****f, ****r;//r=f-Au, u=(Ex,Ey,Ez)^T
  double ***sigma11, ***sigma22, ***sigma33;//electric conductivities
  double ***invmur;//inverse of relative magnetic permeability
} gmg_t;
```

The dimensionalities n1, n2 and n3 must be multiple of a factor of power of 2, in that the size of grid along x, y and z directions must be regularly halved from fine to coarse grid each time, according to the basic principle of GMG method. The maximum number of grid levels is lmax=min(m1,m2,m3) with m1, m2 and m3 being the largest power of 2 as an integer factor of n1, n2 and n3. The electrical conductivities sigma11, sigma22 and sigma33 and the inverse of relative magnetic permeability invmur are 3D arrays of size n1*n2*n3 defined at cell centres. Since a number of frequencies may be simulated over 3D staggered grid, the solution of the Maxwell equation, it's right hand side and the residual of PDE at each grid level are complex-valued 4D arrays stored in gmg[lev].u, gmg[lev].f and gmg[lev].r, where the level index lev ranges from 0 to lmax-1.

The V cycle is the basic building block for multigrid iterative solver. At each level, we first perform v1 times Gauss-Seidel smoothing, then map the residual of the Maxwell equation from current level to a coarser grid using residual(...) and restriction(...). After calling v_cycle(...) recursively, the coarse grid solution supplies a correction term to update the solution at current level thanks to the routine prolongation(...). A post smoothing of v2 times allows V cycle moving to an upper level. This idea has been illustrated in the following.

```
void v_cycle(gmg_t *gmg, int lev)
{

  int n, i;

  if(cycleopt==1 && lev==0){//compute the norm of the residual
    residual(gmg, lev);//residual r=f-Au at lev-th lev
    n = 3*(gmg[lev].n1+1)*(gmg[lev].n2+1)*(gmg[lev].n3+1);
    rnorm = sqrt(creal(inner_product(n, &gmg[lev].r[0][0][0][0], &gmg[lev].r[0][0][0][0])));
    if(verb) printf("icycle=%d rnorm=%e\n", icycle, rnorm);

    if(icycle==0) rnorm0 = rnorm;
    else if(rnorm<rnorm0*tol) { icycle=ncycle; return; }
  }

  for(i=0; i<v1; i++) smoothing(gmg, lev, i);//pre-smoothing of u based on u,f at lev-th level
  if(lev<lmax-1 && gmg[lev+1].sc[0]*gmg[lev+1].sc[1]*gmg[lev+1].sc[2]>1){
    residual(gmg, lev);//residual r=f-Au at lev-th lev
    restriction(gmg, lev);//restrict gmg[lev].r to gmg[lev+1].f

    n = 3*(gmg[lev+1].n1+1)*(gmg[lev+1].n2+1)*(gmg[lev+1].n3+1);
    memset(&gmg[lev+1].u[0][0][0][0], 0, n*sizeof(complex));
    v_cycle(gmg, lev+1);// another v-cycle at (lev+1)-th level

    prolongation(gmg, lev);//interpolate r^h=gmg[lev+1].u to r^2h from (lev+1) to lev-th level
  }
  //if lev==lmax-1, then nx=ny=2, grid size=3*3, only 1 point at the \xch{centre}{center} is \xch{unknown}{unknwn}
  //direct solve (equivalent to smoothing at \xch{centre}{center} point) by one post-smoothing will do the job
  for(i=0; i<v2; i++) smoothing(gmg, lev, i);//post-smoothing
}
```

At the outset of V cycle, the norm of the equation residual $r = b - AE$ has been computed using an inner product between complex-valued vectors. The W and F cycles can then be constructed using V cycle, see w_cycle(...) and f_cycle(...) for implementation details. The F cycle is the default option due to the efficiency of error smoothing, while W cycle is not recommended because of dramatically increased computational cost. In practice, the iterations over V/F cycles will be terminated if the residual is reduced down 6 orders of magnitude.

3.2. Modularized multigrid solver

All the related parameters for multigrid modelling of a particular frequency are initialized by the routine gmg_init(...). The actual modelling will be carried out by calling the routine gmg_apply(...). Note that the input arguments for gmg_apply(...) are rather terse, which may use some parameters from the copy of the pointer emf declared internally thanks to the initialization done by gmg_init(...) at the outset of GMG modelling. This allows us to strictly follow the same argument list every time when a GMG must be performed. Following the same concept, we initialize the pointer emf with emf_init(...) before multigrid modelling and deallocate the memory with emf_close(...) afterwards. Looping over a number of frequencies based on the modularized multigrid solver leads to a rather compact code for CSEM modelling:

```
  for(ifreq=0; ifreq<emf->nfreq; ifreq++){
    emf_init(acq, emf, ifreq);
    gmg_init(emf, ifreq);

    n = 3*emf->n123pad;
    x = alloc1complex(n);//vector E=(Ex,Ey,Ez)^T
    b = alloc1complex(n);//vector Js=(Jx,Jy,Jz)^T
    inject_source(acq, emf, b, ifreq);//initialize b=i*omega*mu*Js
    memset(x, 0, n*sizeof(complex));//initialize x=0

    gmg_apply(n, b, x);//after multigrid convergence, x=(Ex,Ey,Ez)^T

    extract_emf_data(acq, emf, x, b, ifreq);
    extract_emf_field(acq, emf, x, b, ifreq);

    free1complex(x);
    free1complex(b);

    gmg_close();
    emf_close(emf);
  }
```

The modularized programming hides the tedious details of V/F cycles involving Gauss-Seidel smoothing, restriction, prolongation etc. Because of the finite integration formulation, we multiply the cell volume on both sides of the equation. The solution after a number of V/F cycles will be copied into the unknown vector, as demonstrated by the following code snippet.

```
/*< apply multigrid as a linear solver for Ax=b >*/
void gmg_apply(int n, complex *b, complex *x)
{
  int i, j, k;
  int icycle, lev;
  double vol;

  memcpy(&gmg[0].f[0][0][0][0], b, n*sizeof(complex));
  memset(&gmg[0].u[0][0][0][0], 0, n*sizeof(complex));
  for(k=0; k<gmg[0].n3; k++){
    for(j=0; j<gmg[0].n2; j++){
      for(i=0; i<gmg[0].n1; i++){
        //multiply volume
        vol = gmg[0].d1s[i]*gmg[0].d2s[j]*gmg[0].d3s[k];
        gmg[0].sigma11[k][j][i] *= vol;
        gmg[0].sigma22[k][j][i] *= vol;
        gmg[0].sigma33[k][j][i] *= vol;
        gmg[0].invmur[k][j][i] *= vol;
      }
    }
  }
  for(k=0; k<=gmg[0].n3; k++){
    for(j=0; j<=gmg[0].n2; j++){
      for(i=0; i<=gmg[0].n1; i++){
        //multiply volume on both left and right sides
        vol = gmg[0].d1s[i]*gmg[0].d2[j]*gmg[0].d3[k];
        gmg[0].f[0][k][j][i] *= vol;
        vol = gmg[0].d1[i]*gmg[0].d2s[j]*gmg[0].d3[k];
        gmg[0].f[1][k][j][i] *= vol;
        vol = gmg[0].d1[i]*gmg[0].d2[j]*gmg[0].d3s[k];
        gmg[0].f[2][k][j][i] *= vol;
      }
    }
  }

  for(icycle=0; icycle<ncycle; icycle++){
    for(lev=1; lev<lmax; lev++) grid_init(gmg, lev);
    if(cycleopt==1) v_cycle(gmg, 0);
    if(cycleopt==2) f_cycle(gmg, 0);
    if(cycleopt==3) w_cycle(gmg, 0);
    for(lev=1; lev<lmax; lev++) grid_close(gmg, lev);
  }
  memcpy(x, &gmg[0].u[0][0][0][0], n*sizeof(complex));//copy
      E into x
  compute_H_from_E(gmg, 0);//compute H and store it in gmg
      [0].f
  memcpy(b, &gmg[0].f[0][0][0][0], n*sizeof(complex));//copy
      H into b
}
```

In the above code segment, isemicoarsen takes the option 1 (to do semi-coarsening) or 0 (for a full coarsening scheme); tol (with the default value 10^{-6}) is the tolerance criterion for V, W and F cycles. At the end of the code, the electric fields (E_x, E_y, E_z) are copied into the vector x while the magnetic field (H_x, H_y, H_z) (deduced from the electrical fields according to equation (4)) is stored in the vector b.

3.3. Building the inversion gradient

The electrical fields at the nodes of the uniform grid are required to construct the inversion gradient according to (10). They can be extracted using trilinear interpolation. Note that the parallel components of the electrical field E_x, E_y, vertical electrical current J_z and the magnetic components H_x, H_y and H_z are continuous in the presence of conductivity discontinuities. Since interpolation assumes the continuity of a given function, we interpolate over J_z and then convert J_z to E_z component by dividing the conductivities for the nodal values. These are embedded in the routine extract_emf_data(...) and extract_emf_field(...).

The extracted forward and adjoint EM fields on uniform grid for nfreq frequencies will be stored in 4D arrays E1f,E2f,E3f and E1a,E2a,E3a. Consider VTI anisotropy, we end up with fwi->npar=2 parameters (horizontal resistivity $\rho_{11} = \rho_{22}$ and vertical resistivity ρ_{33}) in total. Building the inversion gradient can therefore be achieved by the following code:

```
s = emf->dx*emf->dy*emf->dz;//cell volume
for(k=0; k<fwi->npar; k++){
  for(i3=0; i3<emf->nz; i3++){
    for(i2=0; i2<emf->ny; i2++){
      for(i1=0; i1<emf->nx; i1++){
        fwi->grad[k][i3][i2][i1] = 0;
        for(ifreq=0; ifreq<emf->nfreq; ifreq++){
          if(fwi->idxpar[k]==1) {
            fwi->grad[k][i3][i2][i1] += creal(E1f[ifreq][i3
                ][i2][i1]*E1a[ifreq][i3][i2][i1]);
            fwi->grad[k][i3][i2][i1] += creal(E2f[ifreq][i3
                ][i2][i1]*E2a[ifreq][i3][i2][i1]);
          }
          if(fwi->idxpar[k]==2){
            fwi->grad[k][i3][i2][i1] += creal(E3f[ifreq][i3
                ][i2][i1]*E3a[ifreq][i3][i2][i1]);
          }
        }//end for ifreq
        //convert from dJ/d(sigma) to dJ/dln(rho)
        if(fwi->idxpar[k]==1) fwi->grad[k][i3][i2][i1] *= s/
            emf->rho11[i3][i2][i1];
        if(fwi->idxpar[k]==2) fwi->grad[k][i3][i2][i1] *= s/
            emf->rho33[i3][i2][i1];

        //mute gradient above bathymetry
        if(emf->oz + (i3+0.5)*emf->dz<= emf->bathy[i2][i1]+
            emf->dz) fwi->grad[k][i3][i2][i1] = 0.;
      }//end for i1
    }//end for i2
  }//end for i3
}//end for k
```

Because the model above the sea floor has been filled with sea water whose conductivity/resistivity is known, there is no need to update the parameters for this part throughout the whole inversion. We therefore mute gradient above the seabed, whose depth is specified by the bathymetry emf->bathy. Note that the resistivity parameters are defined at the cell centre. In the vicinity of the source within the radius emf->dsmute, it is important to mute the gradient to prevent the side effect of singular values affecting the model update. Finally, an MPI reduction sums over the local gradient computed from different sources to form the whole gradient of the data misfit.

3.4. Quasi-Newton algorithm

With the gradient at hand, CSEM inversion can estimate an update vector δm according to (8). The limited-memory BFGS (LBFGS) algorithm approximates the inverse Hessian with a matrix B_k up to a scaling factor α_k, so that the minimization updates the inversion parameters

$$m^{k+1} = m^k - \alpha_k B_k \nabla f^k, \tag{16}$$

where $\nabla f^k := \partial f(m)/\partial m|_{m=m^k}$ is the gradient of the misfit at the kth iteration. Define

$$\begin{cases} s_k := & m^{k+1} - m^k, \\ y_k := & \nabla f^{k+1} - \nabla f^k, \\ \rho_k := & 1/(y_k^{\mathrm{T}} s_k), \\ V_k := & I - \rho_k y_k s_k^{\mathrm{T}}. \end{cases} \tag{17}$$

The matrix B_k is constructed using the gradients computed in the previous ℓ iterations [36]

$$\begin{aligned} B_k =& \gamma_k (V_{k-1}^{\mathrm{T}} \cdots V_{k-\ell}^{\mathrm{T}})(V_{k-\ell} \cdots V_{k-1}) \\ &+ \rho_{k-\ell} (V_{k-1}^{\mathrm{T}} \cdots V_{k-\ell+1}^{\mathrm{T}}) s_{k-\ell} s_{k-\ell}^{\mathrm{T}} (V_{k-\ell+1} \cdots V_{k-1}) \\ &+ \cdots + \rho_{k-1} s_{k-1} s_{k-1}^{\mathrm{T}}, \end{aligned} \tag{18}$$

where $\gamma_k = s_{k-1}^{\mathrm{T}} y_{k-1} / y_{k-1}^{\mathrm{T}} y_{k-1}$. Instead of building the matrix B_k explicitly, the action of inverse Hessian matrix applied to the gradient vector, is computed to obtain the descent direction $d_k := -B_k \nabla f^k$ based on the two-loop recursion [36, algorithm 7.4]. In case the norm of the gradient vanishes or no gradient stored in memory at the first iteration, the LBFGS algorithm switches to steepest descent method by using the negative gradient as the descent direction.

```
/*< calculate search direction (two-loop recursion) >*/
```

```c
void lbfgs_descent(int n, float *g, float *d, float **sk, float **yk, float *q, float *rho, float *alpha, opt_t *opt)
{
  int i, j;
  float tmp0, tmp1, gamma, beta;

  //safeguard a descent direction from negative gradient, d =-g
  tmp0=opt->kpair>0?l2norm(n, opt->sk[opt->kpair-1]):0;
  tmp1=opt->kpair>0?l2norm(n, opt->yk[opt->kpair-1]):0;
  if(!( tmp0>0. && tmp1>0.)){
    flipsign(n, g, d); //descent direction= -gradient
    return;
  }

  //store the gradient in vector q
  memcpy(q, g, n*sizeof(float));

  //first loop
  for(i=opt->kpair-1; i>=0; i--){
    // calculate rho
    tmp0=dotprod(n, yk[i], sk[i]);
    tmp1=dotprod(n, sk[i], q);
    rho[i]=1./tmp0;
    alpha[i]=rho[i]*tmp1;
    for(j=0; j<n; j++) q[j] -= alpha[i]*yk[i][j];
  }

  tmp0 = 1./rho[opt->kpair-1];
  tmp1 = dotprod(n, yk[opt->kpair-1], yk[opt->kpair-1]);
  gamma = tmp0/tmp1;//initial Hessian = gamma* I
  for(j=0; j<n; j++) d[j]=gamma*q[j];

  //second loop
  for(i=0; i<opt->kpair; i++){
    tmp0=dotprod(n, yk[i], d);
    beta=rho[i]*tmp0;
    tmp1=alpha[i]-beta;
    for(j=0; j<n; j++) d[j] += tmp1*sk[i][j];
  }

  for(j=0; j<n; j++) d[j]=-d[j];//descent direction = - H^(-1)*g
}
```

In the above, the memory length ℓ is specified by the parameter `opt->kpair`; `l2norm()` and `dotprod()` calculate the L_2 norm of a vector and the dot product between two real-valued vectors, respectively.

3.5. *Bisection-based backtracking line search*

Since the LBFGS algorithm is not scale invariant, we have to determine a proper stepsize α_k by line search method, in order to satisfy the following two Wolfe conditions:

$$f(m^k+\alpha_k d_k) \le f(m^k) + c_1\alpha_k(\nabla f^k)^{\mathrm{T}} d_k, \tag{19a}$$

$$\nabla f(m^k+\alpha_k d_k)^{\mathrm{T}} d_k \ge c_2(\nabla f^k)^{\mathrm{T}} d_k, \tag{19b}$$

where the two constants are taken to be $c_1 = 10^{-4}$ and $c_2 = 0.9$. The condition (19a) ensures that there is sufficient decrease of the misfit, while the condition (19b) enforces a consistency in the curvature to prevent extremely small stepsize.

In practice, we use a bisection strategy to repeatedly shrink the range of a proper stepsize α between a lower bound α_1 and an upper bound α_2, which varies from one iteration to the next. At the outset of line search, we initialize $\alpha_1 = 0$, $\alpha_2 = +\infty$ and $\alpha = 1$. In each iteration, we check the following things in order: If the condition (19a) is violated, the upper bound of α is set to be $\alpha_2 = \alpha$ while we take $\alpha = (\alpha_1+\alpha_2)/2$; otherwise, if the condition (19b) is violated, the lower bound of α is updated to be $\alpha_1 = \alpha$ and a new α is picked up:

$$\alpha = \begin{cases} 2\alpha, & \text{if } \alpha_2 = +\infty \\ \frac{1}{2}(\alpha_1+\alpha_2), & \text{otherwise.} \end{cases} \tag{20}$$

The checking is performed iteratively until the total number of line search `opt->nls` is reached. In practice, it is also important to apply bound constraints (which are determined based on a priori knowledge of physics) in nonlinear optimization. The following code snippet serves as a precise implementation of this bisection line search strategy with bound constraints.

```c
void line_search(int n,//dimension of x
                 float *x,//input vector x
                 float *g,//gradient of misfit function
                 float *d,//descent direction
                 opt_fg fg,//subroutine to evaluate function and gradient
                 opt_t *opt)//pointer of l-BFGS
/*< bisection line search  based on Wolfe condition >*/
{
  int j;
  float gxd, c1_gxd, c2_gxd, fcost, fxx, alpha1, alpha2;
  float *xk;
  static float infinity = 1e10;

  opt->alpha = 1.;
  alpha1 = 0;
  alpha2 = infinity;

  xk = alloc1float(n);//allocate memory for current x
  memcpy(xk, x, n*sizeof(float));//store x at k-th iteration
  //m3=slope of the function of alpha along direction d
  gxd = dotprod(n, g, d);//<G[f(x)]|d>
  c1_gxd = opt->c1*gxd;//c1*<G[f(x)]|d>
  c2_gxd = opt->c2*gxd;//c2*<G[f(x)]|d>
  for(opt->ils=0; opt->ils<opt->nls; opt->ils++){
    for(j=0; j<n; j++) x[j] = xk[j] + opt->alpha*d[j];//update x

    //clip x by lower+upper bounds (l-BFGS-B, bounded l-BFGS)
    if(opt->bound==1) boundx(x, n, opt->xmin, opt->xmax);
    fcost = fg(x, g);//function and gradient evaluation
    opt->igrad++;//update counter of function + gradient evaluation

    //m3=the slope of the function of alpha along search d
    gxd = dotprod(n, g, d);//<G[f(x+alp*d)]|d>
    fxx = opt->fk + opt->alpha * c1_gxd;

    //check Wolfe condition for current step length
    //condition 1: f(x + alp*d) <= f(x) + m1*alpha*<G[f(x)]|d>
    //condition 2: <G[f(x+alp*d)]|d>  >= m2*<G[f(x)]|d>
    if(fcost > fxx){
      if(opt->verb) printf("Wolfe condition 1 fails: insufficient misfit decrease!\n");
      alpha2 = opt->alpha;
      opt->alpha = 0.5*(alpha1+alpha2);//shrink search interval
    }else if(gxd < c2_gxd){
      if(opt->verb) printf("Wolfe condition 2 fails: stepsize is too small!\n");
      alpha1 = opt->alpha;
      if(alpha2<infinity)
        opt->alpha = 0.5*(alpha1 + alpha2);//shrink search interval
      else
        opt->alpha *= 2.0;//extend search interval
    }else{//conditions satisfied, terminate line search
      break;
    }

    if(opt->verb){
      printf("#line search %d, alp1=%f alp2=%f alp=%f\n", opt->ils, alpha1, alpha2, opt->alpha);
      printf("----------------------------------\n");
    }
  }

  if(fcost <= opt->fk) {
    opt->ls_fail = 0;
    opt->fk = fcost;//fcost not increased, accept it
  }else{
    opt->ls_fail = 1; //line search fails, exit
  }

  free1float(xk);
}
```

3.6. Function and gradient evaluation with reverse communication

To build the multigrid module in section 3.2, we have tacitly introduced a new programming paradigm called *reverse communication*. It creates a reliable mechanism, allowing the program easily jumping out and getting back to the same breakpoint without loss any information after the completion of the previous computational segment. This turns out to be critical to design a clean nonlinear inversion scheme, which separates the functionality of quasi-Newton optimization with function and gradient evaluation at each iteration. Indeed, reverse communication has been widely used in Fortran programming [40]. The programmers usually introduce a flag parameter in Fortran to achieve reverse communication: the code calls the same subroutine but taking different values for the flag in order jump out of the computational segment after a while, or jump into it to continue an uncompleted procedure.

Different from Fortran convention, we have decided to separate them in our C code. The module for function and gradient evaluation is divided into three different subroutines:

1. Once the inversion starts, we create local copies of the pointers to access the information of acquisition geometry stored in pointer `acq`, electromagnetic fields indexed by pointer `emf` and inversion parameters linked with the pointer `fwi`, by calling the routine

   ```
   void fg_fwi_init(acq_t *acq_, emf_t *emf_, fwi_t
     *fwi_);
   ```

   which mimics the constructor in C++ class.
2. The nonlinear inversion updates the model parameters iteratively. During each iteration, we resort to the routine

   ```
   float fg_fwi(float *x, float *g)
   ```

   for function and gradient evaluation, where the input model vector and output gradient vector are stored in `x` and `g`, with a returned value being the computed misfit. We highlight that there are many places that require accessing to the pointers `acq`, `emf` and `fwi`, which can be done internally thanks to the local copies of these pointers initialized by `fg_init(...)`. This makes the argument list of `fg_fwi` rather compact so that it would be called frequently among different iterations.
3. At the end of the inversion, the variables used in this module will be deallocated via `fg_close()`, which plays the role of a destructor as in C++ class.

The reverse communication allows us to greatly simplify the preconditioned LBFGS algorithm for nonlinear optimization, as illustrated in the following:

```
for(opt->iter=0; opt->iter<opt->niter; opt->iter++){
  ...
  memcpy(opt->q, opt->g, fwi->n*sizeof(float));
  if(opt->iter==0){/* first iteration, no stored gradient
      */
    if(opt->preco) precondition(emf, fwi, opt->q);
    flipsign(fwi->n, opt->q, opt->d);//descent direction=-
        gradient
  }else{
    lbfgs_update(fwi->n, opt->x, opt->g, opt->sk, opt->yk,
        opt);
    opt->rho = alloc1float(opt->kpair);
    opt->alp = alloc1float(opt->kpair);
    if(opt->preco) {
      lbfgs_descent1(fwi->n, opt->g, opt->q, opt->rho, opt
          ->alp, opt->sk, opt->yk, opt);
      precondition(emf, fwi, opt->q);
      if(opt->loop1) lbfgs_descent2(fwi->n, opt->g, opt->q
          , opt->rho, opt->alp, opt->sk, opt->yk, opt);
    }else
      lbfgs_descent(fwi->n, opt->g, opt->d, opt->sk, opt->
          yk, opt->q, opt->rho, opt->alp, opt);
    free1float(opt->rho);
    free1float(opt->alp);
  }
  lbfgs_save(fwi->n, opt->x, opt->g, opt->sk, opt->yk, opt
      );
  line_search(fwi->n, opt->x, opt->g, opt->d, fg_fwi, opt)
      ;
  ...
}
```

Here, the routine `lbfgs_update(...)` updates the storage to keep only the latest `opt->kpair` pairs of s_k and y_k. The estimation of the descent direction using two-loop recursion LBFGS algorithm by `lbfgs_descent()` can be split into two subroutines `lbfgs_descent1()` and `lbfgs_descent2()`. In between, a preconditioner can be applied to achieve a preconditioned LBFGS implementation. The function name `fg_fwi` has been used as one of the arguments in `line_search` stage, thanks to a function pointer defined in the type of

```
typedef float (*opt_fg)(float*, float*);
```

Putting all these techniques together, Fig. 3 schematically illustrates the complete workflow of 3D CSEM inversion using GMG modelling engine.

4. Numerical examples

4.1. Forward modelling

We now perform a comparative study on the numerical modelling of `libEMMI_MGFD` in a 1D layered resistivity model as shown in Fig. 4. In this simulation, we deploy a x-directed transmitter at the water depth of 950 m, while a line of receivers is placed at the sea floor (50 m below the source). This allows us to check the accuracy of our modelling using 1D semi-analytic solution thanks to the `empymod` program [41]. Because `libEMMI_MGFD` performs the same multigrid modelling as `emg3d` code [25] does, it is also instructive to make a cross-validation among the three. In order to make a fair comparison, we input the resistivity model of exactly the same size (`nx=ny=200`, `nz=100`) and grid spacing (`dx=dy=100`, `dz=40`) for `emg3d` and `libEMMI_MGFD`. The code will make an extended model of proper size for efficient GMG modelling while avoiding the boundary effect.

Fig. 5 shows all the electromagnetic field components after the modelling using `libEMMI_MGFD`. To quantitatively check the amplitude and phase of our modelling, we compare the E_x and H_y component of the EM data recorded by the receivers among `libEMMI_MGFD`, `emg3d` and `empymod` in Fig. 6. We have seen a very good agreement among these three in terms of both amplitude and phase. The phases in Fig. 6b and 6d seem to indicate that compared to the solution from `emg3d`, the solution from `libEMMI_MGFD` is slightly closer to the semi-analytic solution obtained from `empymod`.

Let us also check the computational time and memory consumption between `emg3d` and `libEMMI_MGFD`. To complete the above simulation, both `emg3d` and `libEMMI_MGFD` extend the input model to a size of $256 \times 256 \times 160$ for multigrid solving using semi-coarsening and line relaxation. In terms of CPU time, `emg3d` converges within 16.2 minutes

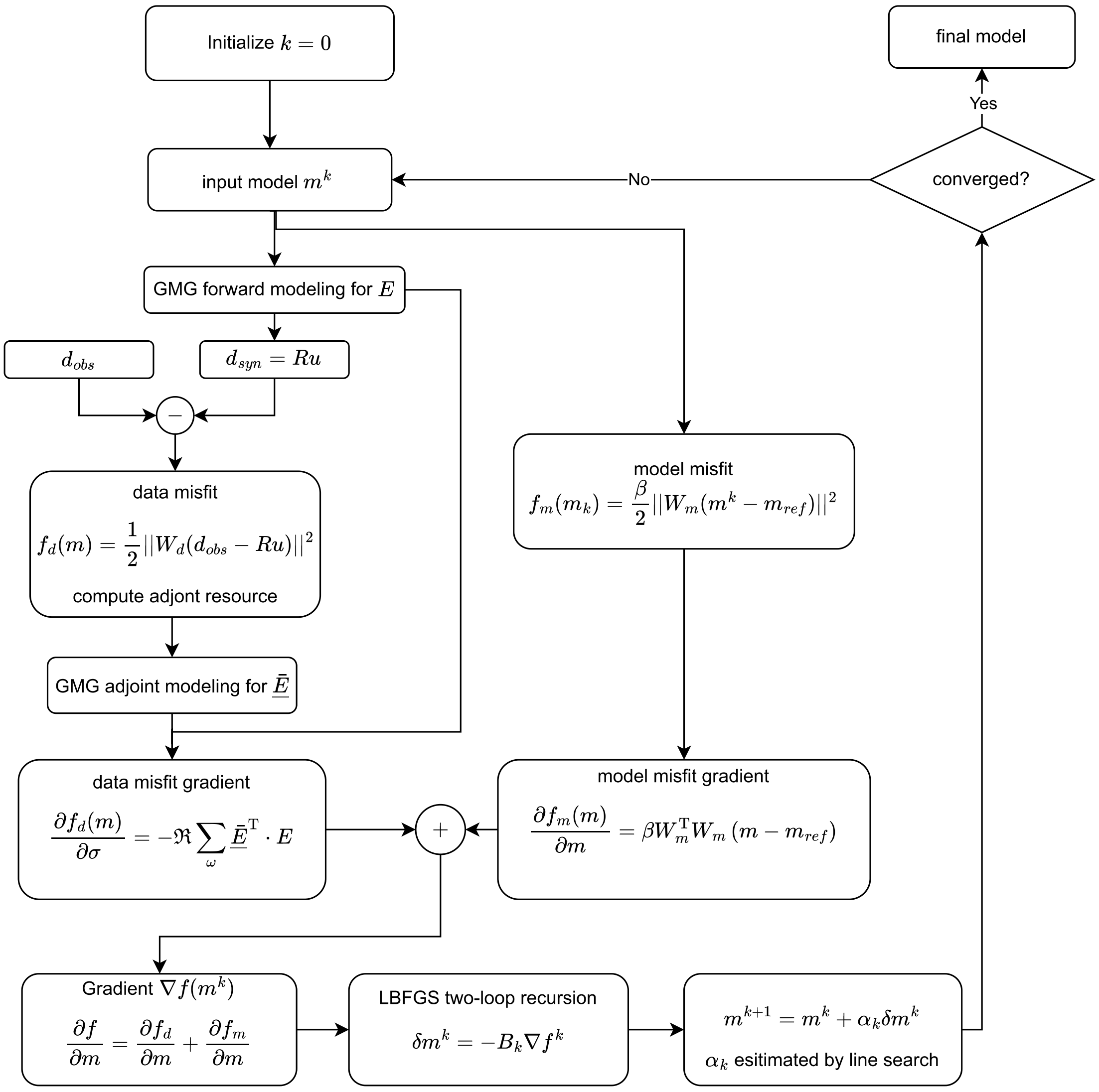

Initialize $k = 0$
final model
Yes
input model m^k
No
converged?
GMG forward modeling for E
d_{obs}
$d_{syn} = Ru$
$-$
data misfit
$f_d(m) = \frac{1}{2}||W_d(d_{obs} - Ru)||^2$
compute adjont resource
model misfit
$f_m(m_k) = \frac{\beta}{2}||W_m(m^k - m_{ref})||^2$
GMG adjoint modeling for $\bar{E}$
data misfit gradient
$\frac{\partial f_d(m)}{\partial \sigma} = -\Re \sum_\omega \bar{E}^T \cdot E$
$+$
model misfit gradient
$\frac{\partial f_m(m)}{\partial m} = \beta W_m^T W_m (m - m_{ref})$
Gradient $\nabla f(m^k)$
$\frac{\partial f}{\partial m} = \frac{\partial f_d}{\partial m} + \frac{\partial f_m}{\partial m}$
LBFGS two-loop recursion
$\delta m^k = -B_k \nabla f^k$
$m^{k+1} = m^k + \alpha_k \delta m^k$
α_k esitimated by line search

Fig. 3. 3D CSEM inversion workflow using frequency-domain GMG modelling.

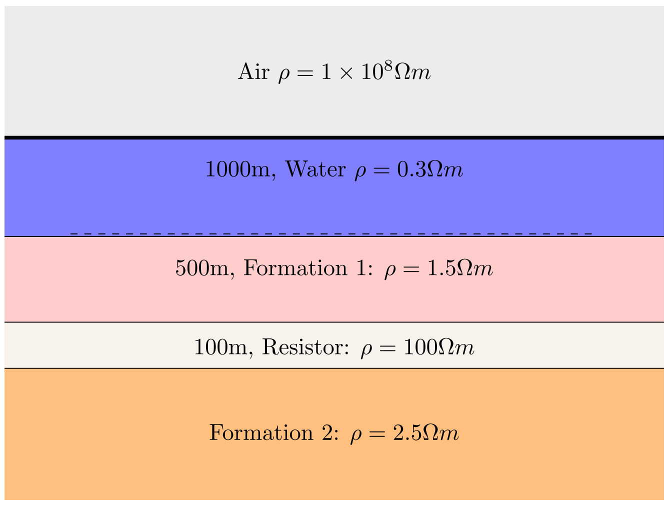

Air $\rho = 1 \times 10^8 \Omega m$
1000m, Water $\rho = 0.3\Omega m$
500m, Formation 1: $\rho = 1.5\Omega m$
100m, Resistor: $\rho = 100\Omega m$
Formation 2: $\rho = 2.5\Omega m$

Fig. 4. The 1D layered resistivity model.

after 13 F cycles, while `libEMMI_MGFD` converges with 14.7 minutes after 30 F cycles. Taking into account the actual number of floating point operations, the computation by `libEMMI_MGFD` coded in C is considered much faster than that of `emg3d` coded in python. This verifies that directly programming in C can still be beneficial in terms of efficiency, while the python programming adding JIT (just-in-time) decorator can create a code with significant speedup so that the performance of the compiled executable is very close to a C/Fortran program of the same functionality. We notice that `libEMMI_MGFD` consumes 3.5 GB memory while `emg3d` only requires 2.8 GB. This may be caused by the fact that `libEMMI_MGFD` uses ILU factorization without exploiting the benefit of symmetry of Cholesky decomposition as done in `emg3d`, besides the additional memory allocation to facilitate inversion.

We now compare the solution of `libEMMI_MGFD` using different gridding strategies by activating automatic gridding using our VTI anisotropic averaging. Fig. 7 shows that the modelled EM fields by VTI anisotropic averaging after regridding the modelling into different number of intervals along z direction still matches the numeric solution without any averaging. However, the simulated EM field via averaging over logarithm of the conductivity proposed in [42] seems to drift away quite a lot, which is very visible in the phase diagram of both electric and magnetic fields.

After confirming the consistency of the modelling using homogenized effective medium, we are now interested in making an assessment of the computationally efficiency gained from regridding the model into a reduced size. Fig. 8a shows that the runtime for modelling grows quickly with the increasing of the mesh size. Meanwhile,

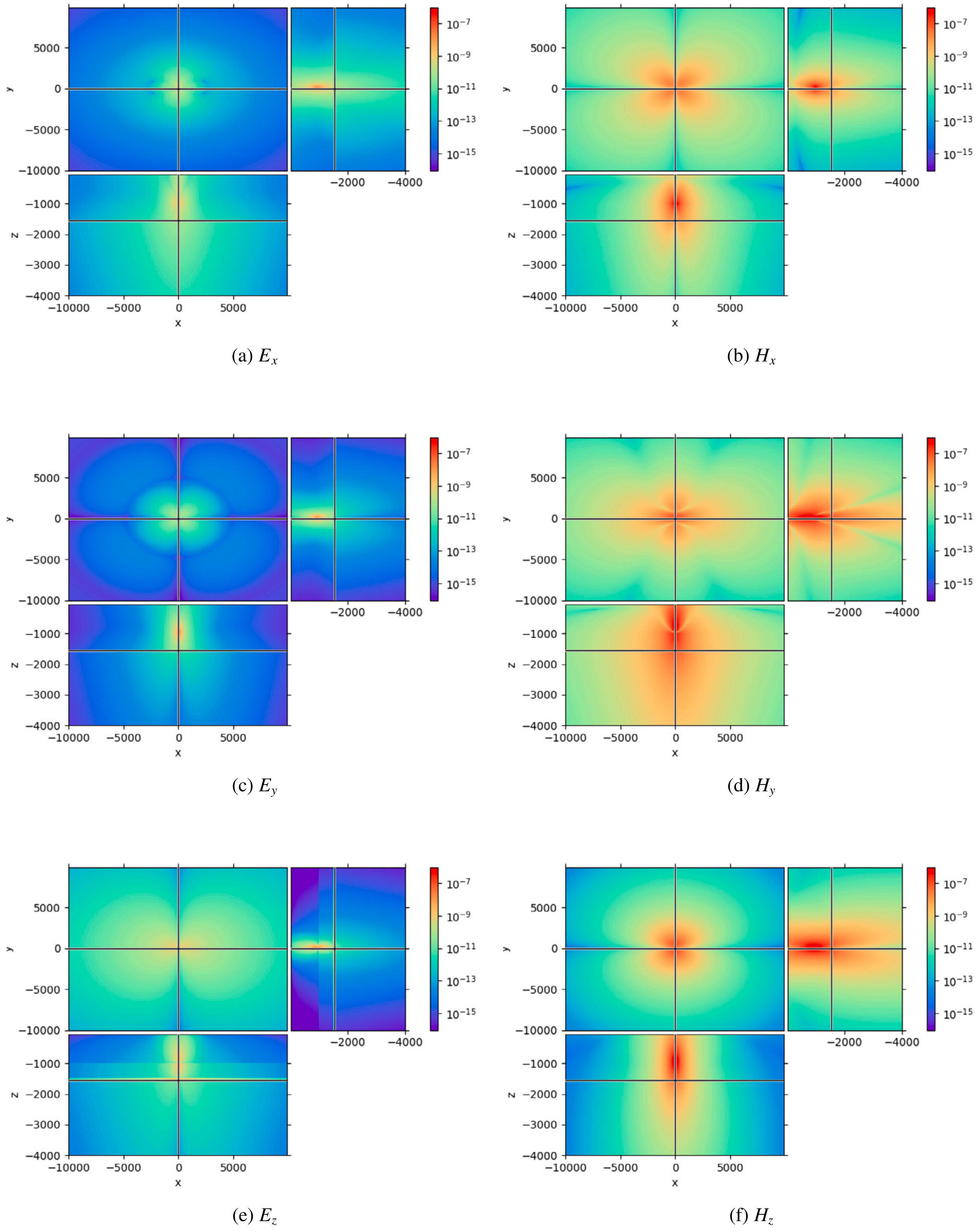

Fig. 5. The amplitude of the EM fields modelled in the 1D layered model.

the consumption of the computer memory exhibits a similar increasing trend as shown in Fig. 8b. These numerical tests suggest that working with the effective medium by VTI anisotropic averaging is advantageous in terms of computational efficiency and memory consumption, as long as the model is regridded properly without loss of too much details.

4.2. *Resistivity imaging*

Using the GMG modelling engine, we perform a synthetic 3D marine CSEM inversion for resistivity imaging. The true model includes two resistors in the shape of a disk (Fig. 9a) and a square (Fig. 9b) sitting at different depth. The model expands horizontally over 20 km in both

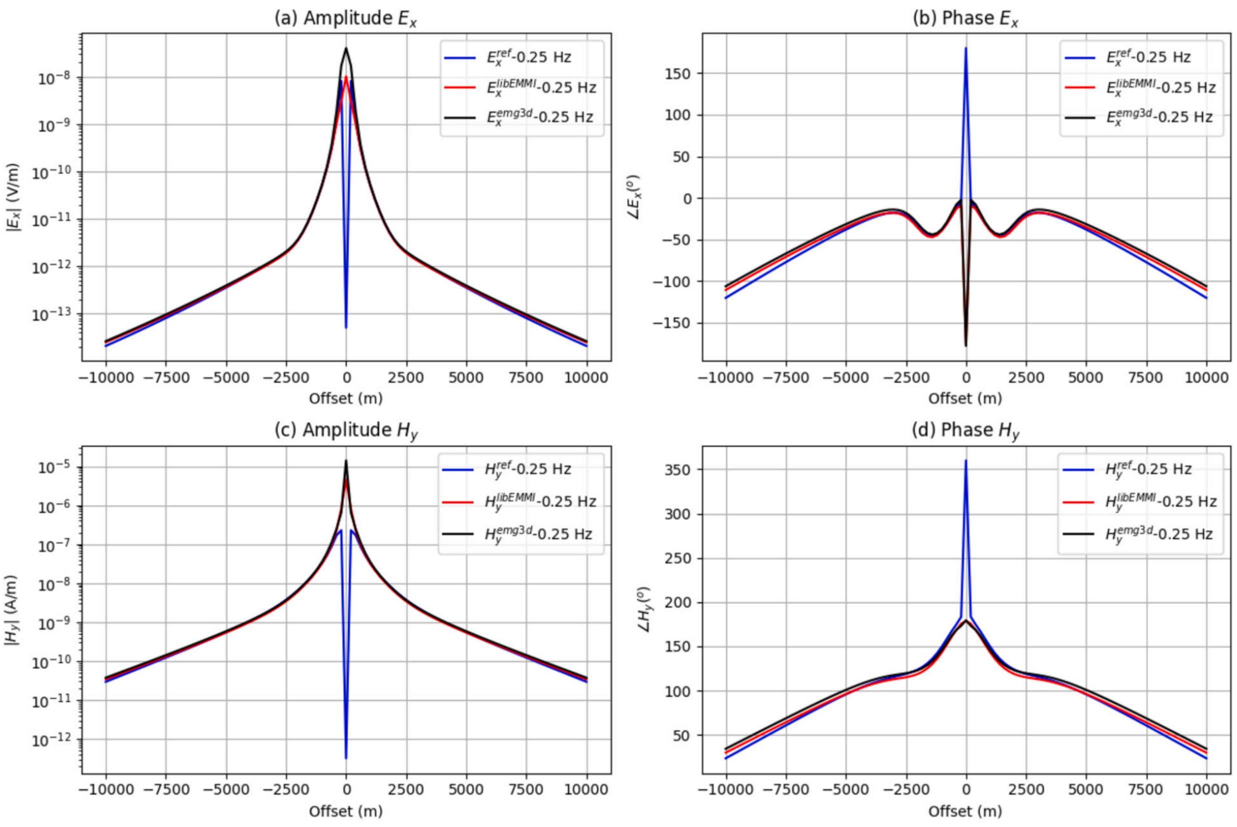

Fig. 6. Comparison between the semi-analytic solution with the numerical solution in a 1D layered model.

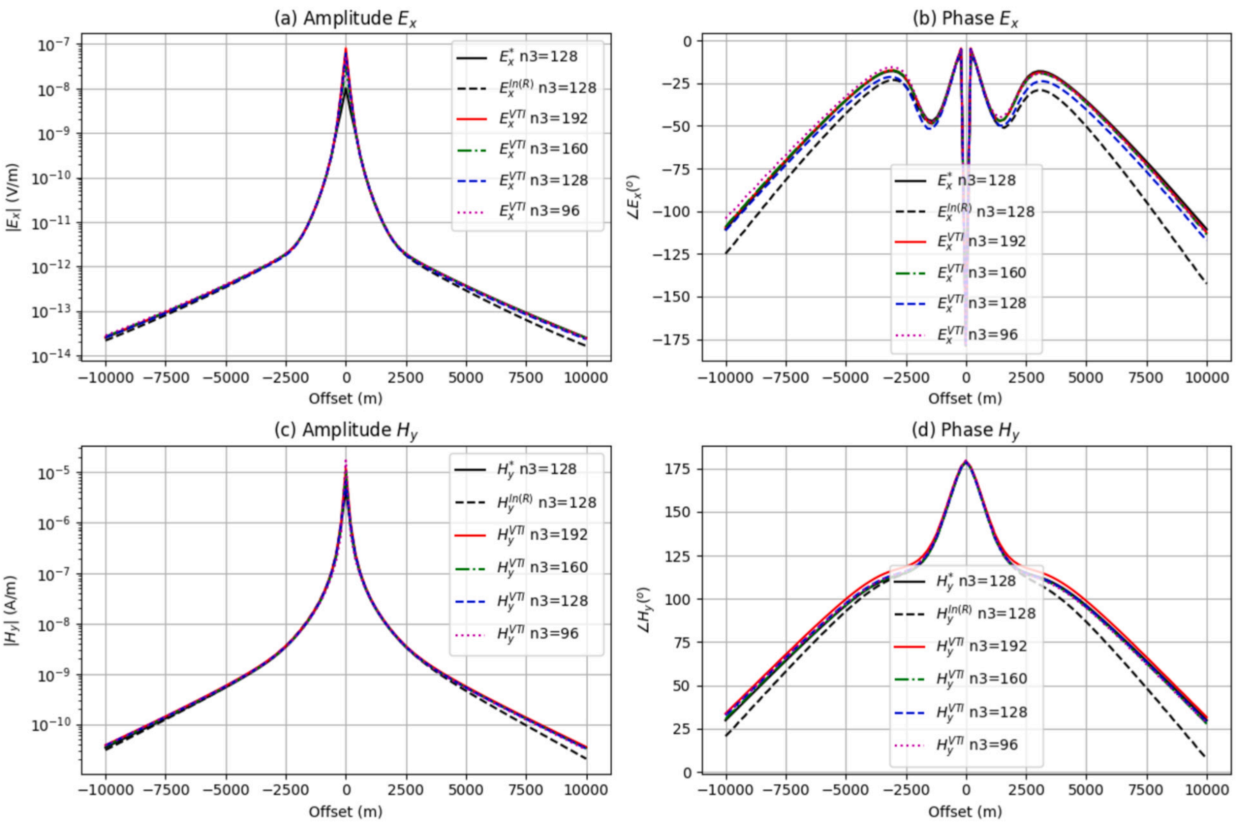

Fig. 7. The simulated EM data using effective medium by gridding the 1D model with different number of intervals in the z direction: E/H superscript * corresponds to the solution without medium homogenization; E/H with superscript VTI are modelled using effective medium by VTI anisotropic averaging; E/H with superscript $\ln(R)$ are modelled using homogenized medium by averaging over logarithm of the conductivity as in [42].

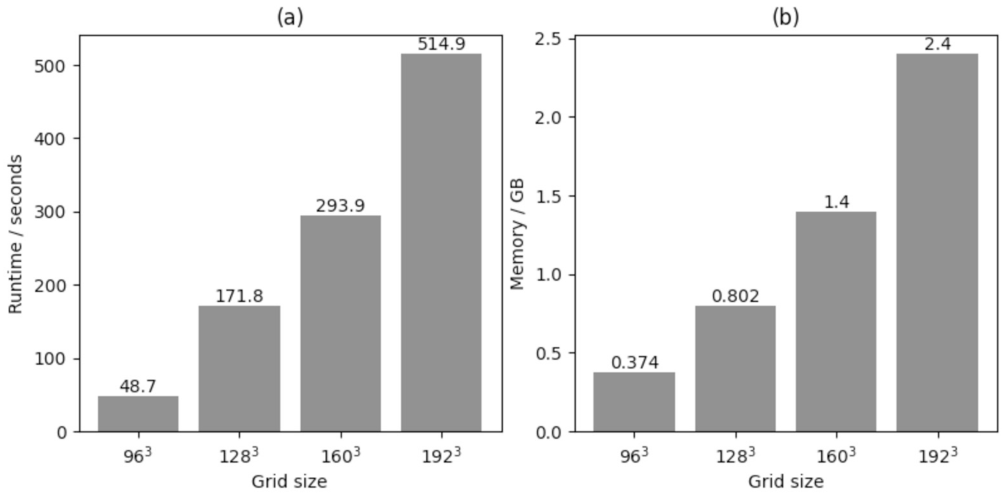

Fig. 8. The runtime and memory for modelling in 1D layered model.

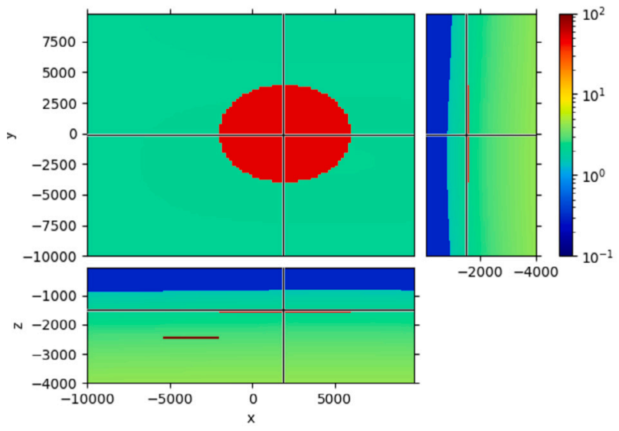

(a)

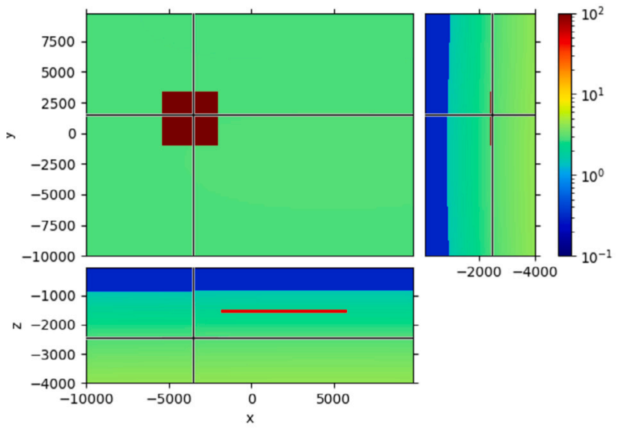

(b)

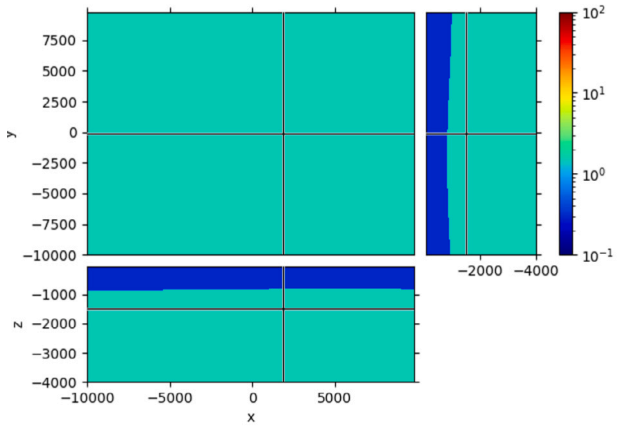

(c)

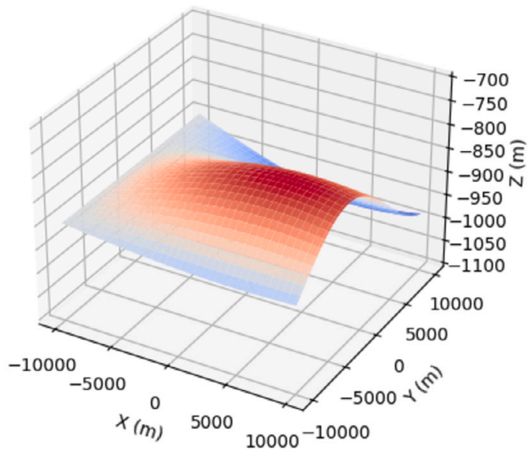

(d)

Fig. 9. The true resistivity model contains two resistors in the shape of disk (a) and square (b), while the initial model takes a homogeneous background of 1.5 $\Omega \cdot m$ below the sea water of 0.3 $\Omega \cdot m$. The sea water and the formation are separated by the bathymetry in (d).

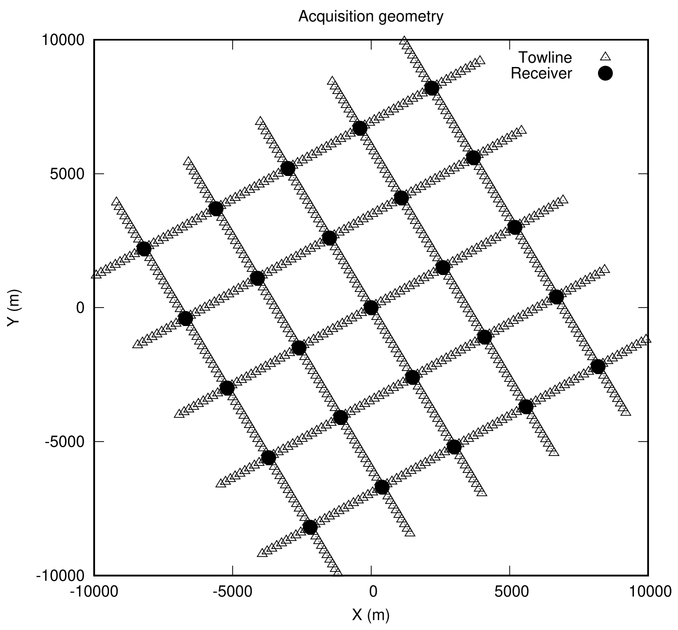

Fig. 10. Survey layout sheet.

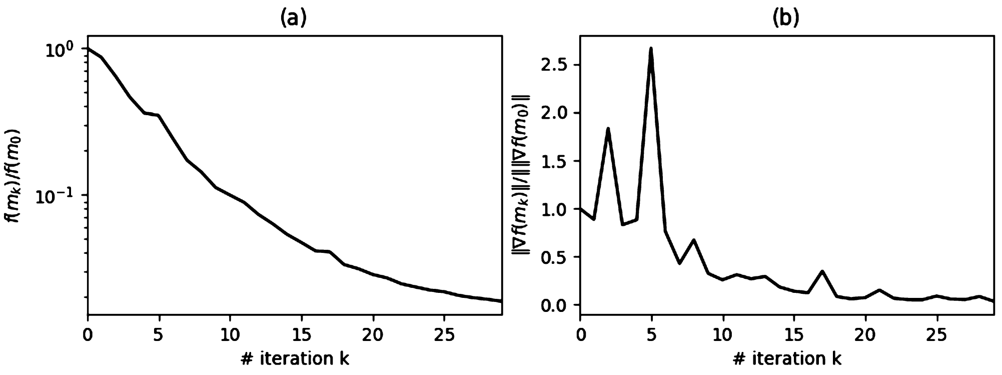

Fig. 11. The evolution of (a) the normalized misfit and (b) the norm of the gradient in CSEM inversion.

x and y directions. We start from a crude initial model with a homogeneous background of 1.5 $\Omega \cdot m$ below the sea water which is of 0.3 $\Omega \cdot m$. The sea water and the sediment of the Earth are separated by a seafloor with depth variations as depicted in Fig. 9d.

To mimic a real acquisition, there are 10 towlines of 16 km deployed: half of the towlines (up to an azimuth angle of 30 degree compared to computing coordinate) are orthogonal to the other ones. In total, 25 sources are places at the cross of the towlines at the seabed. Along each towline, the receivers are distributed with equal spacing of 200 m and at least 50 m above the seabed. Note that the number of sources are much larger than the number of receivers in real CSEM data acquisition. In practice the reciprocity is often applied to form a collection of common receiver gathers as the virtual sources, in order to drastically reduce the computational expense. Our experiment mimics the configuration of imaging the real CSEM data acquired with a source-receiver geometry depicted in Fig. 10 after switching sources and receivers.

We generate the observed data using the true resistivity model for three frequencies: 0.25 Hz, 1.0 Hz and 2.75 Hz. When simulating multiple frequencies, we observed that the GMG solver converges much faster at higher frequencies. This makes sense because the decay rate of the EM fields becomes larger at the higher frequency band.

Using the initial model in Fig. 9c, we run the 3D VTI inversion using LBFGS algorithm for 30 iterations. Since the EM data modelled using a total field approach are not precise at the near offset, the near field within 5.5 skin depth for different frequencies are muted during the inversion. A depth weighting [27] has been used to precondition the LBFGS optimization. Because the energy of the diffusive EM fields decays quickly along the depth, such a weighting helps to boost the weak model update in the depth. The data misfit has been reduced down to less than 2% of the misfit at the 1st iteration, while the norm of the gradient is also greatly reduced, as shown in Fig. 11. The root-mean-square error (RMSE) has been reduced from 8.9 in the first iteration to 1.2 after 30 iterations.

Fig. 12 shows the reconstructed vertical resistivity and horizontal resistivity. Fig. 12a reveals that the resistor in the shallow part has been much better resolved than the deep resistor. Meanwhile, the horizontal resistivity in Fig. 12b seems to show significant amount of update in the background, despite that the resistive anomalies are reconstructed poorly. It is worthy noting that the reconstruction of the resistors in horizontal directions is much better than the vertical direction, in which a strong blurring effect with the increase of the depth in the retrieved resistive anomalies can be observed.

To further check the quality of the data matching, we plotted the RMSE between the observed and synthetic data using the initial model and inverted model in Fig. 13 for all three frequencies corresponding to a source at the centre of the model. Before CSEM inversion, the RMSE misfit for 0.25 Hz, 1 Hz and 2.75 Hz are large, as can be seen from the top panels of Fig. 13. They have been significantly decreased after 3D inversion, as shown in the bottom panels of Fig. 13.

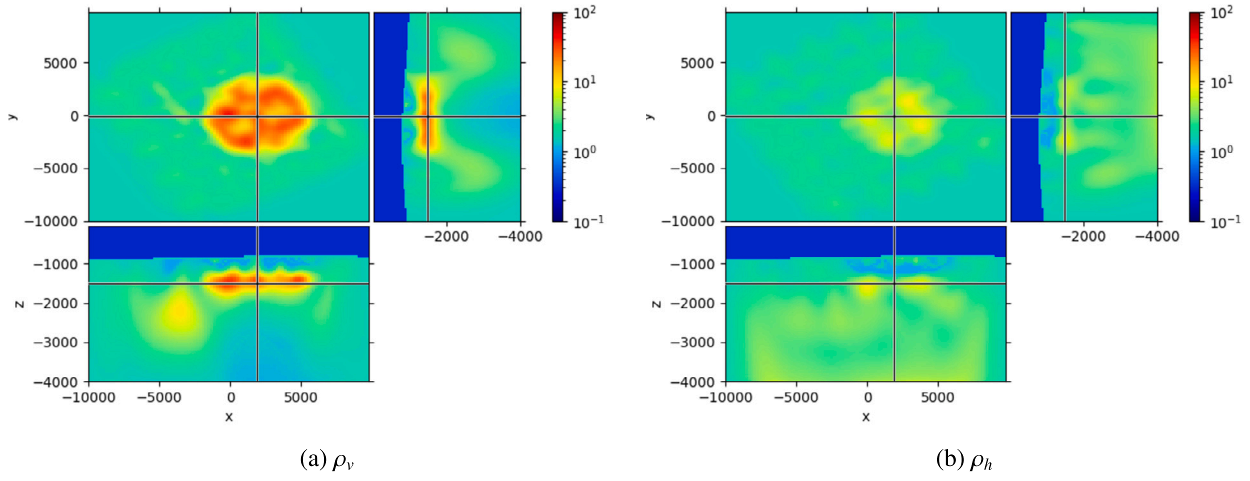

Fig. 12. Inverted resistivity models.

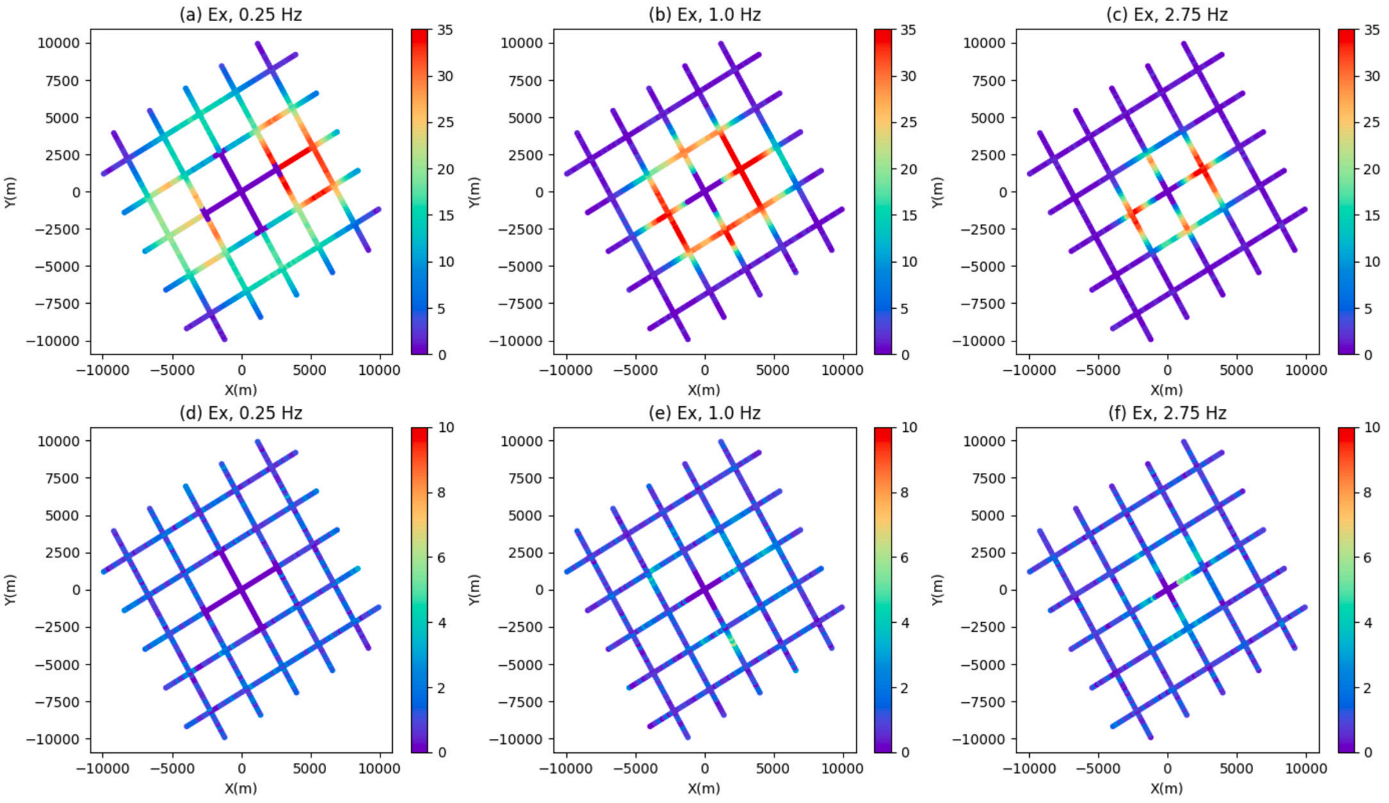

Fig. 13. Comparison of RMSE misfit for a source at the centre of the domain before (a, b, c) and after (d, e, f) 3D CSEM inversion over three frequencies.

5. Discussions

In the current work, we focus on a pure frequency domain solution of diffusive Maxwell equation using multigrid iterative solver. This solver must be performed frequency by frequency in a sequential manner. The benefit of a time domain solver is that it computes all frequencies in one go, but the efficiency of such a scheme strongly depends on the Courant-Friedrichs-Lewy (CFL) stability condition, which limits the size of grid spacing and temporal step size. For 3D resistivity tomography targeting to the oil and gas industry, the CSEM inversion starts with a conductive background model, in which a time domain solver is advantageous. With the evolution of inversion, the model parameters exhibit some resistive anomalies, making the computational efficiency of frequency-domain GMG solver potentially superior to time domain solver. We aim to combine both time and frequency domain approaches into a hybrid scheme for more efficient inversion, by a reorganization of `libEMMI` and `libEMMI_MGFD` in the future.

Motivated by the reduction of memory consumption, BICGSTAB has not been included using GMG as a preconditioner, although it has been recommended by [5]. We realize that the modelling accuracy of current GMG solver needs to be improved further. In a 1D resistivity model, we have observed that the modelling accuracy by current GMG engine is much lower compared to high order fictitious wave domain time-stepping modelling. The accuracy of the electrical field in the current modelling engine is limited to 2nd order accuracy, while the magnetic field is only 1st order. This may be improved by adapting GMG into a higher order scheme in the near future.

Two different sets of grid are sometimes used for 3D CSEM simulation and inversion [27]: The inversion updates the resistivity parameters on a uniform grid where the input parameters are given, while the modelling runs over a nonuniform grid created based on the homogenized effective medium. Since the modelling grid is source dependent and difficult to be consistent, the gradient is therefore built using the extracted EM fields at the inversion grid by interpolation in the modelling grid. Despite the ease of such a configuration in `libEMMI_MGFD` and the efficacy of simulation over nonuniform grid, our numerical experience indicates that a uniform gridding for both modelling and inversion helps avoid some inconsistent model update from different sources and the instability in decreasing the misfit induced by inconsistent gridding, though the computational cost is increased correspondingly. We have also tested `libEMMI_MGFD` by simultaneous inversion of multicomponent CSEM data. Dramatic reduction of the data misfit seems to be more difficult for multicomponent than single component inversion. The inversion produces a resistivity model less satisfactory than the single component inversion presented above. It is expected to be improved by developing a higher order GMG modelling engine.

The Gauss-Newton method (a type of Newton-CG method) is another popular choice in CSEM inversion [43–48]. The Gauss-Newton algorithm requires two levels of nested loops: an inner loop using linear conjugate gradient method to compute the descent direction by iterative solution of the normal equation according to a symmetric positive Hessian matrix, and an outer loop to do nonlinear update for the model properties. In `libEMMI_MGFD`, the subroutine

```
void cg_solve(int n, //dimension of x
       float *x, //input vector x
       float *g, //gradient of misfit function
       float *d, //descent direction
       opt_Hv Hv, //subroutine to evaluation
           function and gradient
       opt_t *opt) //pointer of optimization
```

has been designed to accomplish the inner linear inversion through CG. As long as the Hessian vector product can be computed in a matrix free manner via a dedicated routine of the following form

```
void Hv_fwi(float *x, float *v, float *Hv){ ...}
```

one can perform Gauss-Newton inversion by feeding `cg_solve` with an input parameter wich is the name of the routine of the type

```
typedef void (*opt_Hv)(float*, float *, float*);
```

This Newton-CG method has been investigated in the seismic full waveform inversion settings [35]. The study in [35] shows that the global computational cost of Gauss-Newton method is generally higher than quasi-Newton LBFGS algorithm, despite the improved convergence according to the number of outer loops. The quasi-Newton LBFGS algorithm is therefore chosen as the default optimization method in `libEMMI_MGFD` thanks to its efficiency.

6. Conclusion

We have developed a CSEM modelling and inversion software `libEMMI_MGFD` using a frequency-domain multigrid solver. The multigrid modelling, constructed by V/F cycles involving Gauss-Seidel smoothing, restriction and prolongation phases, has been modularized for compactness and efficiency. The default nonlinear optimization method is LBFGS algorithm assisted with bisection-based line search. A reverse communication mechanism gives great flexibility for function and gradient evaluation. The code is programmed in C and parallelized using MPI to deal with large scale applications for resistivity tomography. Numerical examples are presented to demonstrate the forward simulation and inverse imaging capabilities of `libEMMI_MGFD`. We envision some necessary modifications to process the field data for industrial applications in the future.

CRediT authorship contribution statement

Pengliang Yang: Writing – review & editing, Writing – original draft, Visualization, Validation, Supervision, Software, Resources, Project administration, Methodology, Investigation, Funding acquisition, Formal analysis, Data curation, Conceptualization. **An Ping:** Writing – review & editing, Validation, Software, Methodology.

Declaration of competing interest

The authors declare that they have no known competing financial interests or personal relationships that could have appeared to influence the work reported in this paper.

Data availability

No data was used for the research described in the article.

Acknowledgements

This research is financially supported by National Natural Science Foundation of China (Grant No. 42274156). Pengliang Yang is indebted to Dieter Werthmüller for responsive feedback in last two years to develop the geometrical multigrid code using C programming language. Without his help and the Python code `emg3d`, it is not possible to complete `libEMMI_MGFD` to share with the community.

References

[1] S. Constable, C.J. Weiss, Mapping thin resistors and hydrocarbons with marine EM methods: insights from 1D modeling, Geophysics 71 (2) (2006) G43–G51.
[2] S. Constable, L.J. Srnka, An introduction to marine controlled-source electromagnetic methods for hydrocarbon exploration, Geophysics 72 (2) (2007) WA3–WA12.
[3] G.A. Newman, D.L. Alumbaugh, Frequency-domain modelling of airborne electromagnetic responses using staggered finite differences, Geophys. Prospect. 43 (8) (1995) 1021–1042.
[4] J.T. Smith, Conservative modeling of 3-D electromagnetic fields, Part i: properties and error analysis, Geophysics 61 (5) (1996) 1308–1318.
[5] W. Mulder, A multigrid solver for 3D electromagnetic diffusion, Geophys. Prospect. 54 (5) (2006) 633–649.
[6] R. Streich, 3D finite-difference frequency-domain modeling of controlled-source electromagnetic data: direct solution and optimization for high accuracy, Geophysics 74 (5) (2009) F95–F105.
[7] M.L. Oristaglio, G.W. Hohmann, Diffusion of electromagnetic fields into a two-dimensional Earth: a finite-difference approach, Geophysics 49 (7) (1984) 870–894.
[8] T. Wang, G.W. Hohmann, A finite-difference, time-domain solution for three-dimensional electromagnetic modeling, Geophysics 58 (6) (1993) 797–809.
[9] A. Taflove, S.C. Hagness, Computational Electrodynamics: The Finite-Difference Time-Domain Method, 3rd edition, Artech House, 2005.
[10] R. Mittet, High-order finite-difference simulations of marine CSEM surveys using a correspondence principle for wave and diffusion fields, Geophysics 75 (1) (2010) F33–F50.
[11] Y. Li, K. Key, 2D marine controlled-source electromagnetic modeling: Part 1—an adaptive finite-element algorithm, Geophysics 72 (2) (2007) WA51–WA62.
[12] N.V. da Silva, J.V. Morgan, L. MacGregor, M. Warner, A finite element multifrontal method for 3D CSEM modeling in the frequency domain, Geophysics 77 (2) (2012) E101–E115.
[13] K. Key, MARE2DEM: a 2-D inversion code for controlled-source electromagnetic and magnetotelluric data, Geophys. J. Int. 207 (1) (2016) 571–588.
[14] R. Rochlitz, N. Skibbe, T. Günther, custEM: customizable finite-element simulation of complex controlled-source electromagnetic data, Geophysics 84 (2) (2019) F17–F33.
[15] A.V. Grayver, R. Streich, O. Ritter, Three-dimensional parallel distributed inversion of CSEM data using a direct forward solver, Geophys. J. Int. 193 (3) (2013) 1432–1446.
[16] H. Cai, B. Xiong, M. Han, M. Zhdanov, 3D controlled-source electromagnetic modeling in anisotropic medium using edge-based finite element method, Comput. Geosci. 73 (2014) 164–176.
[17] J.T. Smith, Conservative modeling of 3-D electromagnetic fields, Part II: biconjugate gradient solution and an accelerator, Geophysics 61 (5) (1996) 1319–1324.

[18] V. Puzyrev, J. Koldan, J. de la Puente, G. Houzeaux, M. Vázquez, J.M. Cela, A parallel finite-element method for three-dimensional controlled-source electromagnetic forward modelling, Geophys. J. Int. 193 (2) (2013) 678–693.
[19] E. Haber, S. Heldmann, An octree multigrid method for quasi-static Maxwell's equations with highly discontinuous coefficients, J. Comput. Phys. 223 (2) (2007) 783–796.
[20] J. Koldan, V. Puzyrev, J. de la Puente, G. Houzeaux, J.M. Cela, Algebraic multigrid preconditioning within parallel finite-element solvers for 3-d electromagnetic modelling problems in geophysics, Geophys. J. Int. 197 (3) (2014) 1442–1458.
[21] P. Yang, R. Mittet, Controlled-source electromagnetics modelling using high order finite-difference time-domain method on a nonuniform grid, Geophysics 88 (2) (2023) E53–E67, https://doi.org/10.1190/geo2022-0134.1.
[22] P. Yang, 3D fictitious wave domain CSEM inversion by adjoint source estimation, Comput. Geosci. 180 (2023) 105441, https://doi.org/10.1016/j.cageo.2023.105441.
[23] R. Cockett, S. Kang, L.J. Heagy, A. Pidlisecky, D.W. Oldenburg, SimPEG: an open source framework for simulation and gradient based parameter estimation in geophysical applications, Comput. Geosci. 85 (2015) 142–154.
[24] C. Rücker, T. Günther, F.M. Wagner, pygimli: an open-source library for modelling and inversion in geophysics, Comput. Geosci. 109 (2017) 106–123.
[25] D. Werthmüller, W. Mulder, E. Slob, emg3d: a multigrid solver for 3D electromagnetic diffusion, J. Open Sour. Softw. 4 (2019) 1463, https://doi.org/10.21105/joss.01463.
[26] G. Blanchy, S. Saneiyan, J. Boyd, P. McLachlan, A. Binley, Resipy, an intuitive open source software for complex geoelectrical inversion/modeling, Comput. Geosci. 137 (2020) 104423.
[27] R.E. Plessix, W.A. Mulder, Resistivity imaging with controlled-source electromagnetic data: depth and data weighting, Inverse Probl. 24 (2008) 034012.
[28] W.L. Briggs, V.E. Henson, S.F. McCormick, A Multigrid Tutorial, second edition, Society for Industrial and Applied Mathematics, 2000.
[29] E. Haber, U. Ascher, D. Aruliah, D. Oldenburg, Fast simulation of 3D electromagnetic problems using potentials, J. Comput. Phys. 163 (1) (2000) 150–171, https://doi.org/10.1006/jcph.2000.6545.
[30] C.J. Weiss, Project APhiD: a Lorenz-gauged A-ϕ decomposition for parallelized computation of ultra-broadband electromagnetic induction in a fully heterogeneous Earth, Comput. Geosci. 58 (2013) 40–52, https://doi.org/10.1016/j.cageo.2013.05.002.
[31] Y. Saad, Iterative Methods for Sparse Linear Systems, SIAM, Philadelphia, 2003.
[32] R. Barret, M. Berry, T.F. Chan, J. Demmel, J. Donato, J. Dongarra, V. Eijkhout, R. Pozo, C. Romine, H. Van der Vorst, Templates for the Solution of Linear Systems: Building Blocks for Iterative Methods, SIAM, Philadelphia, PA, 1994.
[33] T. Jönsthövel, Improvement of a multigrid solver for 3D EM diffusion, Master's thesis, Delft University of Technology, 2006.
[34] P. Yang, libEMM: a fictious wave domain 3D CSEM modelling library bridging sequential and parallel GPU implementation, Comput. Phys. Commun. 288 (2023) 108745, https://doi.org/10.1016/j.cpc.2023.108745.
[35] P. Yang, R. Brossier, L. Métivier, J. Virieux, W. Zhou, A time-domain preconditioned truncated Newton approach to visco-acoustic multiparameter full waveform inversion, SIAM J. Sci. Comput. 40 (4) (2018) B1101–B1130.
[36] J. Nocedal, S.J. Wright, Numerical Optimization, 2nd edition, Springer, 2006.
[37] R.E. Plessix, A review of the adjoint-state method for computing the gradient of a functional with geophysical applications, Geophys. J. Int. 167 (2) (2006) 495–503.
[38] R. Mittet, J.P. Morten, Detection and imaging sensitivity of the marine CSEM method, Geophysics 77 (6) (2012) E411–E425.
[39] P. Yang, SMIwiz: an integrated toolbox for multidimensional seismic modelling and imaging, Comput. Phys. Commun. 295 (2024) 109011, https://doi.org/10.1016/j.cpc.2023.109011, https://www.sciencedirect.com/science/article/pii/S0010465523003569.
[40] A. Markus, Modern Fortran in Practice, Cambridge University Press, 2012.
[41] D. Werthmüller, An open-source full 3D electromagnetic modeler for 1D VTI media in Python: empymod, Geophysics 82 (6) (2017) WB9–WB19, https://doi.org/10.1190/geo2016-0626.1.
[42] R.-E. Plessix, M. Darnet, W. Mulder, An approach for 3d multisource, multifrequency csem modeling, Geophysics 72 (5) (2007) SM177–SM184.
[43] M. Li, A. Abubakar, J. Liu, G. Pan, T.M. Habashy, Three-dimensional regularized Gauss-Newton inversion algorithm using a compressed implicit Jacobian calculation for electromagnetic applications, in: SEG International Exposition and Annual Meeting, SEG, 2010, pp. SEG–2010.
[44] M. Zaslavsky, V. Druskin, A. Abubakar, T. Habashy, V. Simoncini, Large-scale Gauss-Newton inversion of transient csem data using the model order reduction framework, Geophysics 78 (4) (2013) E161–E171.
[45] E. Haber, C. Schwarzbach, Parallel inversion of large-scale airborne time-domain electromagnetic data with multiple octree meshes, Inverse Probl. 30 (5) (2014) 055011.
[46] R. Peng, X. Hu, 3D inversion of marine controlled-source electromagnetic data using an inexact Gauss Newton method, in: SEG Technical Program Expanded Abstracts 2015, Society of Exploration Geophysicists, 2015, pp. 1001–1005.
[47] M. Amaya, K. Hansen, J. Morten, 3D CSEM data inversion using Newton and Halley class methods, Inverse Probl. 32 (5) (2016) 055002.
[48] R. Mittet, A. Avdeeva, Gauss-Newton inversion with node-based basis functions: application to imaging of seabed minerals in an area with rough bathymetry, Geophysics 89 (1) (2024) E13–E29.